Research Article

Nitride-reinforced HfNbTaTiV high-entropy alloy with excellent room and elevated-temperature mechanical properties

Bingjie Wang [a], Qianqian Wang [a,b], Bo Sun [a], Jinyong Mo [c], Yangbin Guo [a], Xiubing Liang [c,*], Baolong Shen [a,*]

[a] School of Materials Science and Engineering, Jiangsu Key Laboratory for Advanced Metallic Materials, Southeast University, Nanjing 211189, China
[b] School of Materials Science and Engineering, Jiangsu Key Laboratory of Advanced Structural Materials and Application Technology, Nanjing Institute of Technology, Nanjing 211167, China
[c] Defense Innovation Institute, Academy of Military Science, Beijing 100071, China

ARTICLE INFO

ABSTRACT

Nitride-reinforced $(HfNbTaTiV)_{90}N_{10}$ high-entropy alloy aiming at high-temperature applications is designed in this paper. Abundant FCC nitride phases are formed *in situ* in theBCC matrix by arc melting technique, without complex deformation or heat treatment. The $(HfNbTaTiV)_{90}N_{10}$ alloy exhibits a remarkable yield strength of 2716 MPa and ultimate compressive strength of 2833 MPa with a plastic strain of 10% at room temperature. Besides, the alloy remains a high yield strength of 279 MPa at 1400 °C. The nitride phases play an essential role in maintaining the excellent strength-ductility combination at room temperature and enhancing the high-temperature softening resistance. Alternating BCC and FCC phases possess the semi-coherent interface, which not only strengthens the BCC matrix but also promotes the compatible deformation of the duplex microstructure. The lattice coherency structure of the semi-coherent interface is conducive to the slip transfer of partial dislocations through the interface, which facilitates the accommodation of plastic deformation. The cross-slip of the screw dislocations effectively eliminates stress concentration and leads to good ductility of the dual-phase alloy. The results demonstrate that the nitride phases achieve coordinate deformation with the matrix without deteriorating the ductility of the $(HfNbTaTiV)_{90}N_{10}$ alloy.

© 2023 Published by Elsevier Ltd on behalf of The editorial office of Journal of Materials Science & Technology.

1. Introduction

Refractory high-entropy alloys (RHEAs) with body-centered-cubic (BCC) structures are promising high-temperature materials owing to their excellent softening resistance. However, most RHEAs that can withstand softening at 1400 °C usually suffer from brittleness at room temperature, which leads to poor processability and limits their applications as high-temperature structural materials [1,2]. For instance, although the MoNbTaW RHEA possesses a high strength of 421 MPa at 1400 °C [1], it displays brittle fracture at room temperature. HfNbTaTiZr has a low density and shows good ductility at room temperature, making it a competitive high-temperature material. However, the relatively low strength at room and elevated temperature of HfNbTaTiZr RHEA limits its applications [3]. Some studies have been carried out to overcome the shortcoming of this HEA system. The room-temperature tensile

strength of TiZrHfNb HEA was enhanced from 776 to 1110 MPa after introducing ordered oxygen complexes in the alloy matrix [4]. Our previous work demonstrated that the addition of Al_2O_3 particles dramatically enhanced the strength of the HfNbTaTiZrV to 2700 MPa at room temperature and 693 MPa at 1000 °C [5]. However, the plastic strain of this Al_2O_3-reinforced HfNbTaTiZrV is only 6% at room temperature. The incoherent interface between the oxide and matrix not only decreases the ductility but also limits the doping amount of Al_2O_3 particles. Therefore, a new strategy needs to be developed to design RHEAs with low density to achieve a balance of high strength and ductility at both room and elevated temperatures.

Recent studies have shown that dual-phase materials have more privilege in overcoming the strength-ductility trade-off than single-phase materials [6–12]. Layered eutectic alloy $AlCoCrFeNi_{2.1}$ consists of alternating soft face-centered-cubic (FCC) and hard B_2 phases and exhibits a remarkable strength-ductility combination, with an ultimate tensile strength of 1.2 GPa and elongation of 12% [13]. Through deformation and heat treatment, the $L2_1$ phase with a coherent interface with the BCC matrix formed along the de-

---

formed shear band in CoNiV medium-entropy alloy, making the alloy ultrastrong and ductile [14]. However, due to the high stacking fault energy and the intrinsic brittleness, the above methodology to improve the mechanical performance of FCC HEAs is not suitable for the BCC RHEAs. Some investigations have drawn attention to the addition of the ceramic phase in RHEAs. Ceramic particles such as carbides and nitrides have the intrinsic characteristics of high melting point and strength, which are suitable for ultrahigh temperature applications. It can be introduced into RHEAs as a candidate material to improve the high-temperature softening resistance in extreme conditions. However, poor coordination of the interface between the ceramic particles and the matrix is likely to be the origin of crack initiation.

The key to further improving the strength and conquering severe brittleness is the content of the ceramic phase and the doping method. A feasible method is to promote the *in-situ* precipitation of the secondary phase that possesses a coherent or semi-coherent orientation relationship with the matrix, which can effectively reduce the elastic mismatch energy between precipitates and matrix, and thus increases the interaction of dislocations due to the low interface energy [14]. For instance, a large amount of C element was introduced into the NbMoTaW RHEA to fabricate a dual-phase $Re_{0.5}MoNbW(TaC)_{0.5}$ high-entropy composite with lamellar structures *in situ*, and the carbides possess the semi-coherent interface with the matrix [15]. Combining the advantages of HEAs and carbides, the $Re_{0.5}MoNbW(TaC)_{0.5}$ possesses a high yield strength of 1340 MPa and ultimate compressive strength of 2347 MPa with plasticity of 8.90% at ambient temperature. A similar investigation has been conducted in the $C_x(NbMoTaW)_{100-x}$ alloy, the strength and ductility of NbMoTaW alloy were improved dramatically due to the precipitation of the carbide phase [2]. The nitride has a similar melting point to that of the carbide. Current investigations of nitride-reinforced HEAs are about the interstitial strengthening brought by a trace amount of addition and show the same effects as the C element [4,16,17]. However, the effects of the high content of nitride phase in RHEAs fabricated by arc melting have not yet been reported. Designing dual-phase RHEA with coherent nitride phases is a promising approach to developing materials with excellent high-temperature softening resistance, as well as large room-temperature strength and ductility.

Here we design a nitride-reinforced HfNbTaTiV alloy that can be strengthened through the formation of a semi-coherent interface between the nitride phase and the matrix. The alloy exhibits high strength and large ductility at room temperature, as well as superior high-temperature strength. Detailed microstructural investigations are performed to unveil the origins of the mechanical behavior. The coherent interface relationship between the FCC nitride phase and BCC phase provides a basis for designing high-strength ductile HEAs.

2. Experimental

The ingots were fabricated by arc-melting a mixture of pure metals (purity >99.9 wt%) for the HfNbTaTiV sample and high-purity HfN (99.9 wt%) for the nitride-reinforced $(HfNbTaTiV)_{90}N_{10}$ sample in a vacuum induction melting furnace under argon atmosphere. Each ingot was remelted six times to obtain a uniformly distributed composition. The phase constitution of the alloy was analyzed by X-ray diffractometer (XRD, Bruker D8-Discover) with Cu $K\alpha$ radiation in a 2θ range from 20° to 100° Morphology and grain size distribution were characterized via a field emission scanning electron microscope (SEM, Sirion) equipped with an electron back-scattering diffraction (EBSD) system. The EBSD specimens were prepared by the Vibratory polisher (Buehler VibroMet 2) for 6 h. The EBSD data was analyzed using the Channel 5 software. The Microstructure of the as-cast and fractured spec-

imens was characterized by scanning transmission electron microscopy (STEM, Talos F200X). STEM-High-angle annular dark field (STEM-HAADF) images were recorded using an annular-type detector with a collection semi-angle ~100–269 mrad. Elemental mappings of the samples were acquired by energy-dispersive X-ray spectroscopy (EDX). Samples for compression tests were cut to a dimension of Φ 2 mm × 4 mm using electrical discharging wire-cutting and polished using SiC paper. Room-temperature compression tests were conducted at a crosshead strain rate of 1×10^{-3} s^{-1} using a Sans machine (5305), while the high-temperature compression tests were performed using a Zwick machine (KAPPA 100) with the strain rate of 1×10^{-3} s^{-1} under argon atmosphere. Nano-indentation tests were performed at room temperature using a Nano-indentation tester (NanoTest Vantage) at a maximum load of 15 mN with a loading time of 10 s in load-controlled mode. A 10 μm interval was adopted to exclude possible overlap of the deformed zone produced by the adjacent indentations.

3. Results

3.1. Microstructure and orientation relationship

XRD patterns of the as-cast HfNbTaTiV and nitride-reinforced alloy with the nitrogen content ranging from 2 to 12 at.% are shown in Figs. 1(a) and S1 in the Supporting Information. HfNbTaTiV alloy shows a single BCC structure, while the nitride-reinforced HfNbTaTiV is composed of BCC and FCC phases. The peak positions of the nitride-reinforced alloy move towards a higher value, indicating a decrease in the average lattice spacing of the matrix. This may result from the atoms with larger radii in HfNbTaTiV participating in the formation of the FCC phase. $(HfNbTaTiV)_{90}N_{10}$ alloy is chosen as a representative for microstructure characterization after nitrogen addition. The calculation of phase diagrams for the $(HfNbTaTiV)_{90}N_{10}$ alloy is based on thermodynamic equilibrium using the Thermo-Calc software and the TCHEA database. The calculated phase diagram is shown in Fig. 1(b), FCC phase starts to precipitate at the liquidus temperature of 2750 K. As the liquidus temperature decreases to 2260 K, the BCC phase begins to form, Liquid → FCC + BCC. The liquidus disappears at 2100 K. Hereafter, the alloy is in the stable two-phase field. Besides, the BCC and FCC phases show similar volume fractions. SEM-BSE images of the HfNbTaTiV and $(HfNbTaTiV)_{90}N_{10}$ alloys are shown in Fig. 1(c, d), respectively. There is obvious dendrite segregation in the interior of BCC grains marked by red arrows. As illustrated in Fig. 1(d), the FCC grains exhibit a bimodal size distribution for the fine needle and blocky phases in the $(HfNbTaTiV)_{90}N_{10}$ alloy. An enlarged view of the needle FCC1 phase is shown in the illustration. Abundant needle FCC1 phases are evenly distributed in the matrix. No dendrite segregation is observed within the BCC grains. Here we name the needle and the blocky FCC as FCC1 and FCC2, respectively. The volume fraction of BCC, FCC1, and FCC2 phases of $(HfNbTaTiV)_{90}N_{10}$ alloy measured by Image-Pro-Plus software are 52 vol.%, 26 vol.%, and 22 vol.%, respectively. It is consistent with the theoretical value of the phase fraction.

Fig. 2 shows the EBSD images for the investigated samples. Since the step size of EBSD mapping is 100 nm, the FCC1 phase was not detected in Fig. 2. Phase compositions of the as-cast HfNbTaTiV and $(HfNbTaTiV)_{90}N_{10}$ alloys are shown in Fig. 2(a, b), respectively. As shown in Fig. 2(a), HfNbTaTiV alloy exhibits BCC phase only, which is consistent with the XRD results. According to the phase map in Fig. 2(b), the $(HfNbTaTiV)_{90}N_{10}$ alloy consists of BCC and blocky FCC2 phases. The addition of nitrogen caused significant grain refinement and the grain size of the BCC grain reduced from 89 to 30 μm. Moreover, the BCC matrix and FCC2 show a Kurdjumov-Sachs (K-S) orientation relationship marked by the red lines. The special orientation relationship of the heteroge-
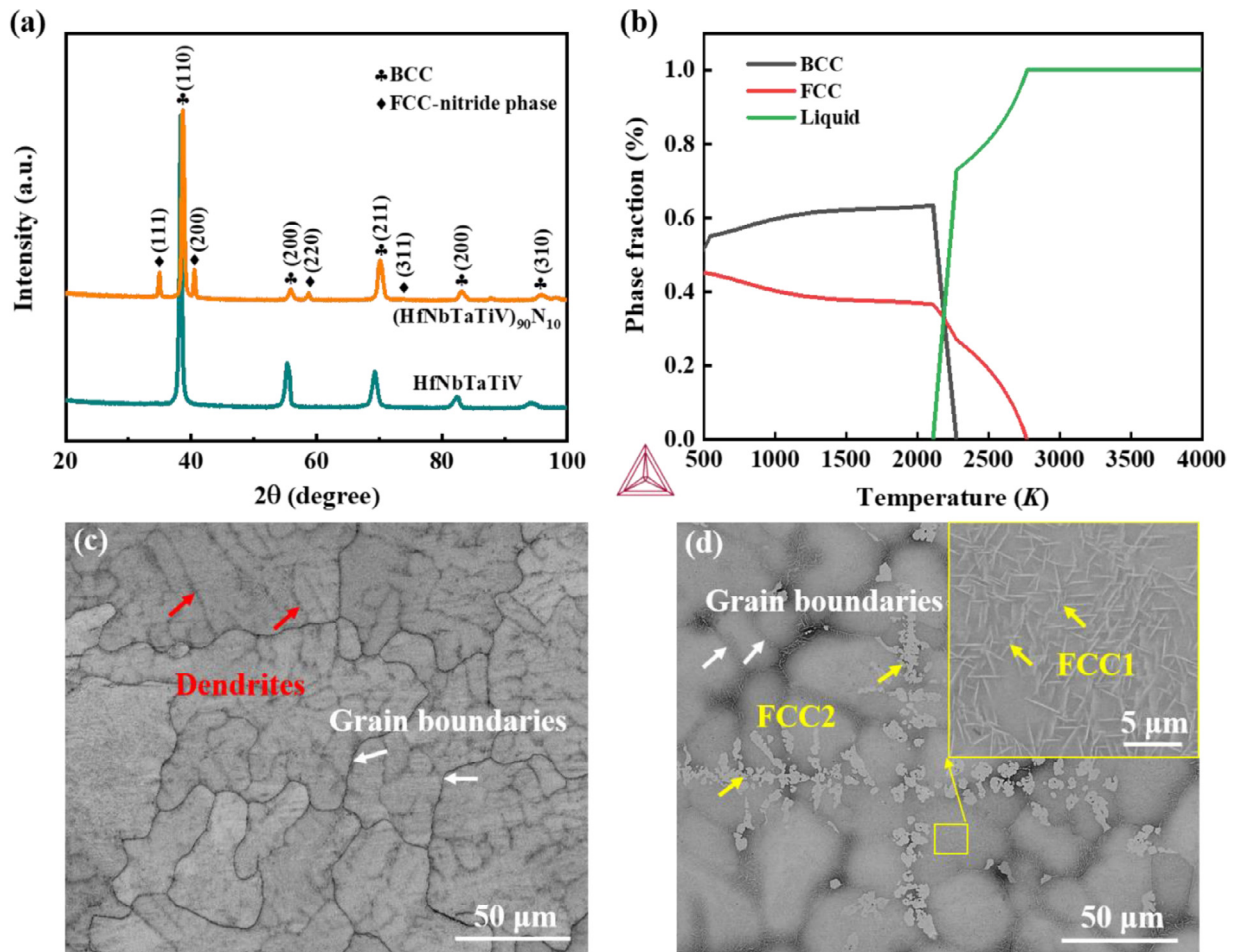
Fig. 1. Phase and microstructure characterization. (a) XRD patterns, (b) calculated equilibrium phase diagrams of the (HfNbTaTiV)$_{90}$N$_{10}$ alloy, (c, d) SEM-BSE images of the as-cast HfNbTaTiV and (HfNbTaTiV)$_{90}$N$_{10}$ alloys, respectively.

neous interface between metal and nitride can effectively reduce the interface energy and improves the coordinated deformation ability [18–20]. It can be proved by the value of kernel average misorientation (KAM), which coincides with the distribution of dislocations. As seen in Fig. 2(c, d), both the as-cast HfNbTaTiV and (HfNbTaTiV)$_{90}$N$_{10}$ exhibit high KAM values near the grain boundary. The high value of KAM is attributed to the increase in local misorientation that is formed due to dislocation accumulation into the lattice, whereas the value is relatively small at the K-S interface between the BCC and blocky FCC2 phases [14,21].

The nanostructure of the as-cast (HfNbTaTiV)$_{90}$N$_{10}$ alloy is examined by TEM. Fig. 3(a) shows the bright-field TEM micrograph of the alternate BCC and FCC1 phases. Corresponding EDX maps are presented in Fig. 3(b). The BCC phase is enriched with Nb, Ta, V, and a small amount of N elements, while the FCC1 nitride is partitioned by Hf, Ti, and N elements. Because the atomic size of Hf is larger than other elements, the average lattice spacing of the BCC matrix is decreased as indicated by the XRD results. As shown in Fig. 3(c), in order to reveal the interface structure of BCC and FCC1 phases, high resolution transmission electron microscopy (HRTEM) is used to analyze the interface marked by the red rectangle area in Fig. 3(a). The selected area electron diffraction (SAED) pattern is given in Fig. 3(d). It is noted that the orientation between the BCC matrix and FCC1 phases is close to the K-S crystallographic relationship while the (011)$_{BCC}$//(200)$_{FCC1}$, [01$\bar{1}$]$_{BCC}$//[001]$_{FCC1}$ with a mismatch angle of about 4.6°. Fig. 3(e) illustrates the inverse Fast Fourier Transformation (IFFT) image of the interface of the

BCC/FCC1 phase marked by a white square in Fig. 3(c), the interplanar distance $d_{(011)}$ = 0.241 nm for the BCC phase approximates to that of the $d_{(200)}$ = 0.228 nm for the FCC1 phase. The mismatch parameter δ between (011)$_{BCC}$ matrix and (200)$_{FCC1}$ nitride is calculated by the following equation:

$$\delta = \frac{2(a_\alpha - a_\beta)}{a_\alpha + a_\beta} \tag{1}$$

Here, a_α and a_β represent the lattice constants of phase on both sides of the phase interface, $a_\alpha > a_\beta$. The calculated mismatch parameter δ is 0.06, which validates the typical semi-coherent structure of the interface. Compared with the incoherent interface, the atomic arrangement on the semi-coherent interface is more ordered, which is conducive to reducing the interface energy. The small mismatch is beneficial to coordinate the two-phase lattice constants and ensure the bonding stability of the interface. Misfit dislocations can be observed in the interface, which interacts with the piled-up dislocations and induces interfacial strengthening.

TEM analyses of the BCC and FCC2 phases of the as-cast (HfNbTaTiV)$_{90}$N$_{10}$ are given in Fig. 4. Fig. 4(a) displays the STEM-HAADF image of the BCC and FCC2 phases viewed along [001]$_{BCC}$ and [011]$_{FCC}$ zone axes. As shown in Table S1, the FCC2 phase is rich in the Hf, Ti, and N elements, and shows a similar composition to that of the FCC1 phase. The HRTEM image of the red rectangle in Fig. 4(a) is shown in Fig. 4(b), revealing the interface of the two phases viewed along the [001]$_{BCC}$//[011]$_{FCC}$ direction. The SAED pattern in Fig. 4(c) reveals the interface between the FCC2 and BCC

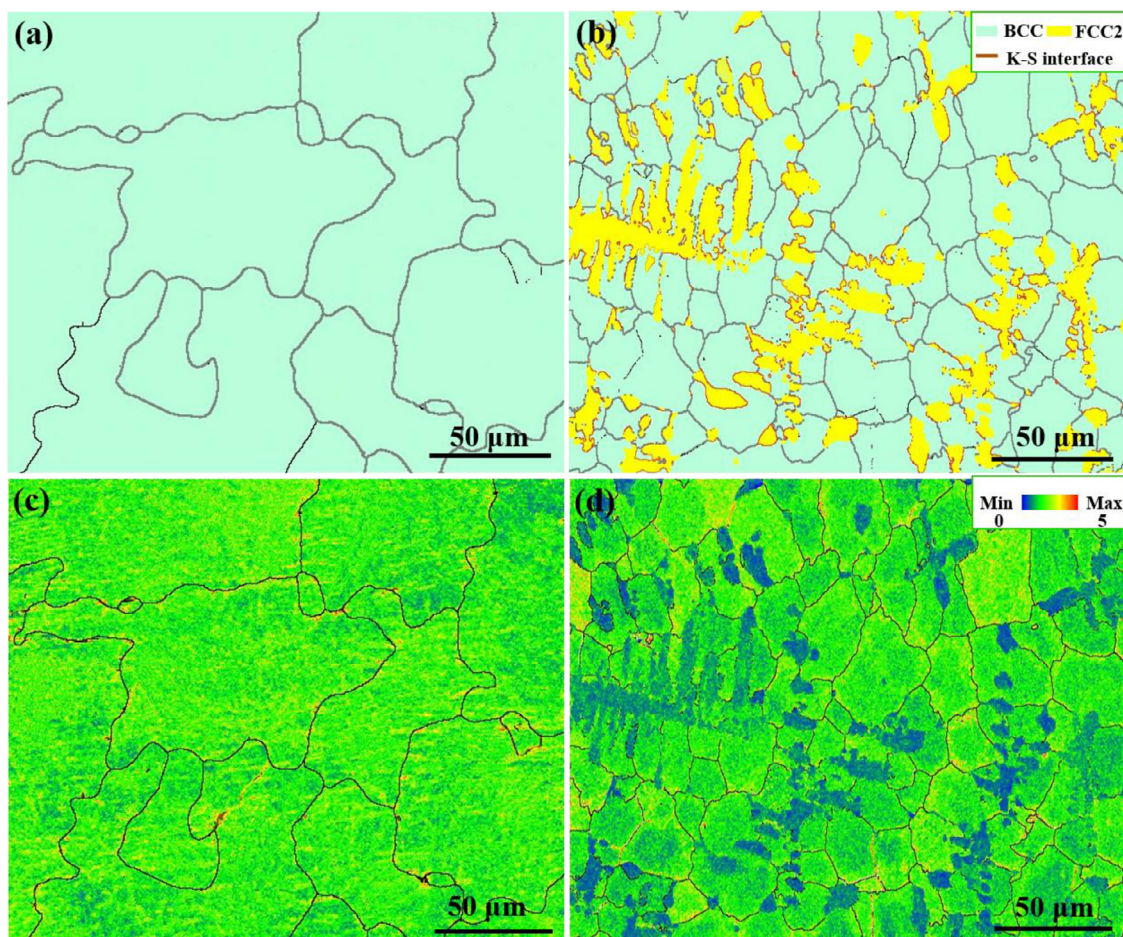**Fig. 2.** EBSD images of the as-cast HfNbTaTiV and (HfNbTaTiV)$_{90}$N$_{10}$ alloys. (a, b) Phase maps, (c, d) Kernel average misorientation (KAM) maps.

phases also satisfies the K-S orientation i.e. $(110)_{BCC}//(111)_{FCC2}$, $111_{BCC}//110_{FCC2}$. The atomic strain distribution map of horizontal normal strain is shown in Fig. 4(d). Due to the mismatch of the atomic radius caused by nitrogen atoms, substantial atomic strain fluctuations exist in the (HfNbTaTiV)$_{90}$N$_{10}$. Although the distribution of atomic strain fields appears random at the nanoscale, which presumably leads to large local internal stresses and thus resistance to dislocation glide [22,23]. The above results prove that both FCC1 and FCC2 phases have K-S orientation relationship and semi-coherent interface with the BCC matrix with the BCC phase.

3.2. Mechanical properties

Figs. 5(a) and S2 show the compressive engineering stress-strain curves of the HfNbTaTiV and nitride-reinforced alloys at various temperatures. At ambient temperature, the HfNbTaTiV alloy depicts low yield strength of 1036 MPa with plasticity exceeding 30%. The strength of the alloy improves dramatically with the addition of nitrogen and reaches the maximum with 10 at.% nitrogen doping. Although the ductility decreases with nitrogen addition, a plastic strain of 10% is still acceptable for engineering applications. With the further addition of nitrogen to 12 at.%, not only the ductility decreases, but the strength of the alloy also decreases. Thus, the (HfNbTaTiV)$_{90}$N$_{10}$ alloy shows the optimal combination of yield strength of 2716 MPa and plastic strain of 10%. The existence of semi-coherent nitrides enhances the yield strength nearly three times compared to the HfNbTaTiV alloy while maintaining good ductility. The mechanical properties and volume fraction of the BCC and FCC phases with various nitrogen content are summa-

rized in Table S2. The origin of the deteriorated mechanical property of the (HfNbTaTiV)$_{88}$N$_{12}$ is the high volume fraction of the coarse FCC2 phase.

Furthermore, (HfNbTaTiV)$_{90}$N$_{10}$ possesses a high yield strength of 639 MPa at 1200 °C and 279 MPa at 1400 °C. To evaluate the phase stability of the (HfNbTaTiV)$_{90}$N$_{10}$ alloy at high temperatures, annealing tests at 1400 °C for 2 and 6 h were conducted. The XRD patterns in Fig. S3(a) demonstrate that the (HfNbTaTiV)$_{90}$N$_{10}$ alloy maintains the same phase structure before and after the annealing. SEM image in Fig. S3(b) shows the microstructure of the alloy annealing at 1400 °C for 6 h. The alloy keeps the same phase structure after annealing for 6 h, which indicates the good phase stability of the alloy at high temperature and reveals the coarsening of FCC1 phase in the grain boundaries is caused by the coupling interaction of high temperature and deformation.

Fig. 5(b) compares the mechanical performance at room temperature of the (HfNbTaTiV)$_{90}$N$_{10}$ alloy with other HEAs that have been reported. It clearly indicates that our study has overcome the disadvantage of precipitation strengthening [2,24–30]. The yield strength is almost twice of other reported single or duple HEAs and still maintains remarkable ductility. The lamellar carbide phases are usually on a micron scale [24,31]. In this work, the nanoscale FCC1 phases are evenly distributed in the (HfNbTaTiV)$_{90}$N$_{10}$ alloy, which produces higher precipitation strengthening than that of the carbide phases. Therefore, the strength and hardness of the alloy are significantly improved. It produces a higher precipitation-strengthening effect. Therefore, the strength and hardness of the alloy are significantly improved. The hardness of the Re$_{0.5}$MoNbW(TaC)$_x$ (x = 0–0.6) alloy ranges from
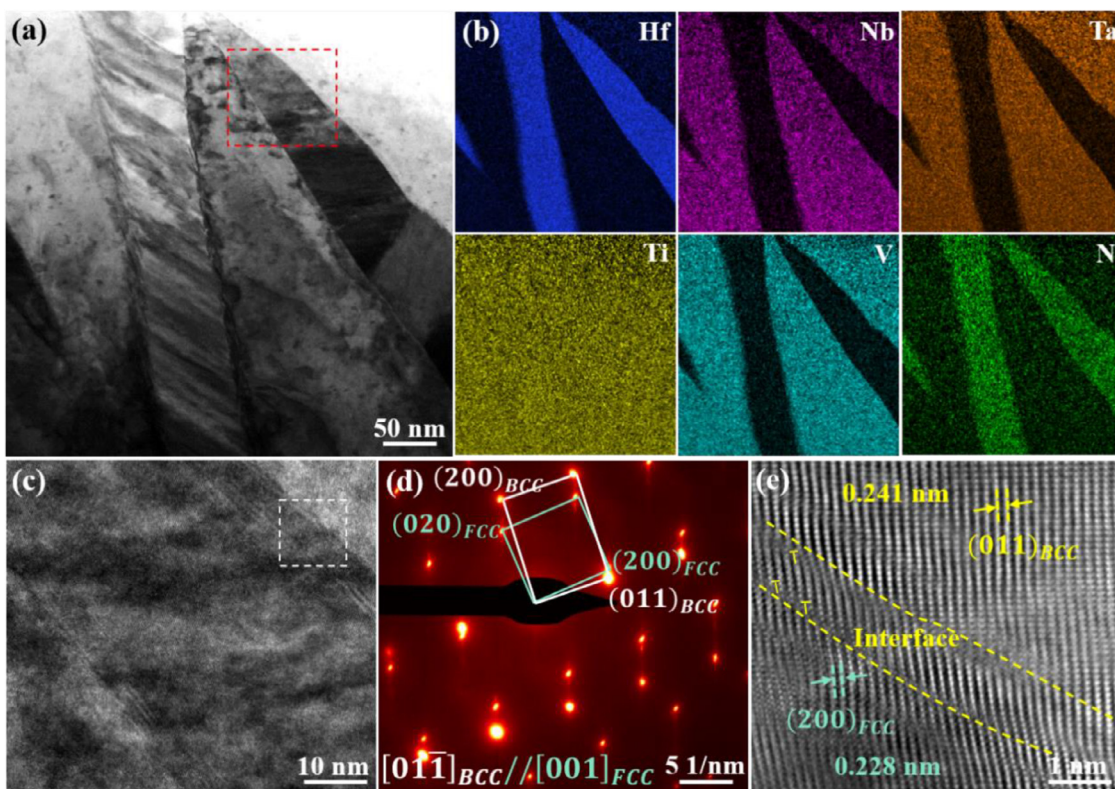
Fig. 3. Microstructure of the as-cast (HfNbTaTiV)$_{90}$N$_{10}$ alloy. (a) Bright-field TEM image, (b) the corresponding EDX maps of (a), (c) HRTEM image and (d) the SAED pattern of the BCC and FCC1 phases, (e) IFFT image of the white square in (c) shows the interface between the BCC and FCC1 phases.
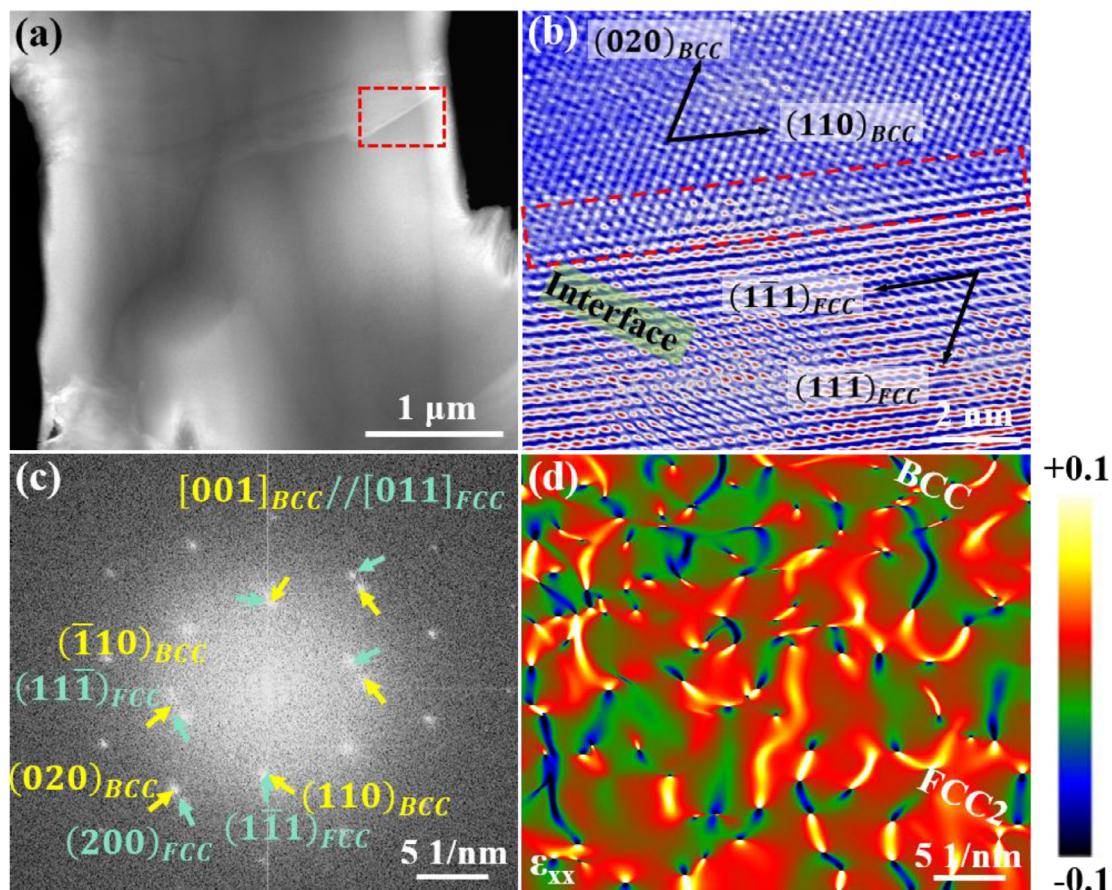

Fig. 4. STEM images of the as-cast (HfNbTaTiV)$_{90}$N$_{10}$ alloy. (a) HAADF-STEM, (b) HRTEM image of red rectangle in (a) shows the interface of the BCC and FCC2 phases, (c) FFT pattern of (b), (d) atomic strain distribution map of horizontal normal strain.
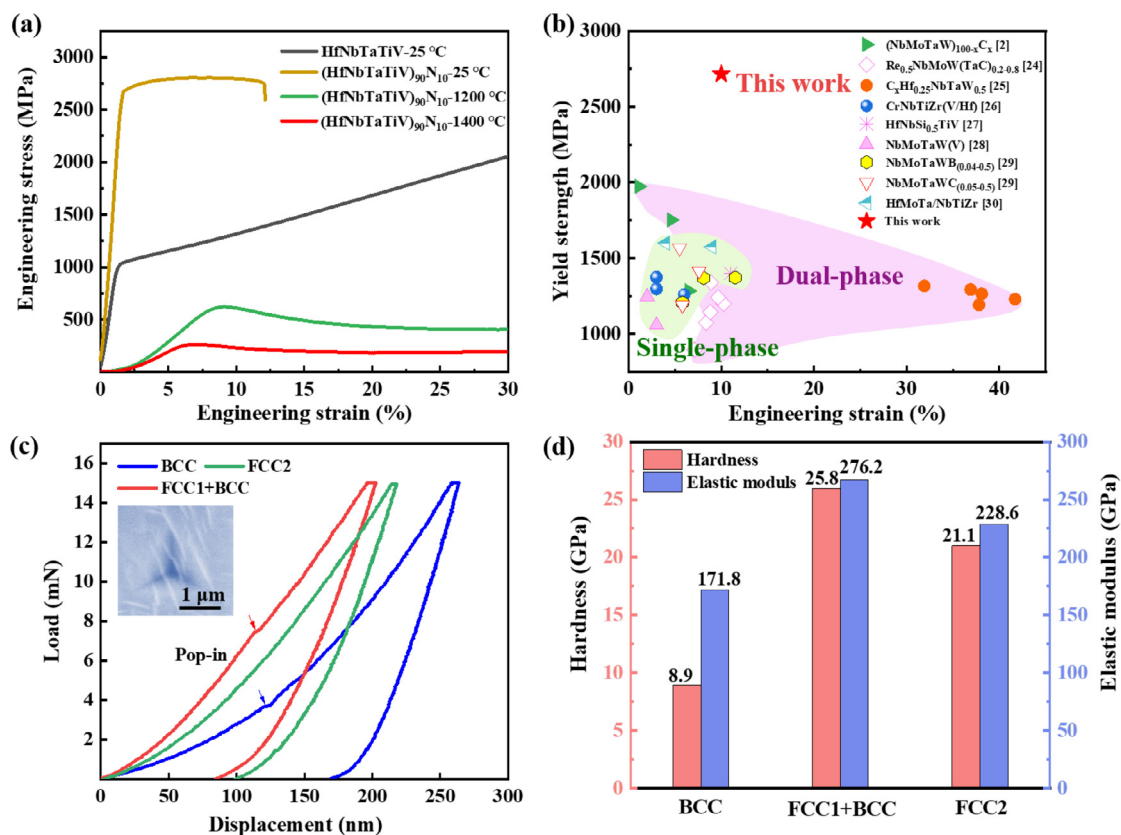
Fig. 5. Mechanical properties. (a) Compressive engineering stress-strain curves of the HfNbTaTiV at ambient temperature and $(HfNbTaTiV)_{90}N_{10}$ at various temperatures, (b) a general summary of the compressive properties of RHEAs with single or duple phases at room temperature, (c) representative load-displacement curves of the $(HfNbTaTiV)_{90}N_{10}$ alloy shows pop-in events at room temperature, (d) hardness and elastic modulus obtained from nanoindentation tests.

472 to 615 HV [31], while the $(HfNbTaTiV)_{90}N_{10}$ alloy exhibits a higher average hardness of 861 HV. Additionally, the substantial hard FCC1 phase in the soft BCC matrix imparts an additional rigid deformation constraint to BCC grain [32]. This high-density phase interface significantly improves the deformation resistance, making dislocations difficult to move in BCC grains until FCC1 phases start to yield. Therefore, the alloy shows a remarkable yield strength. Moreover, compared with the RHEAs that can withstand high-temperature compression at 1400 °C, such as NbMoTaW [1], NbMoTaWV [1], and $(NbMoTaW)_{100-x}C_x$ [2], etc., the $(HfNbTaTiV)_{90}N_{10}$ not only shows higher strength and ductility but also has the lowest density (10.56 g cm^{-3}) due to the addition of Ti. It presents the possibility of developing lightweight RHEAs with high strength and sufficient ductility in the application of room and high temperatures.

Typical load-displacement (*P-h*) curves obtained from nanoindentation tests of $(HfNbTaTiV)_{90}N_{10}$ at areas with different phases, including BCC, FCC1 + BCC, and FCC2 are shown in Fig. 5(c). The SEM image of the indent on the FCC1 + BCC phases is shown in the inset of Fig. 5(c) for clarification. Apparent discrete bursts of displacement termed "pop-in" can be observed in the *P-h* curves of the BCC and BCC + FCC1 phases. The appearance of the first pop-in phenomenon is mainly related to the sudden activation and proliferation of dislocations in the grains. In addition, it represents the onset of the incipient plasticity, indicating that the grains begin to yield and enter an elastic-plastic state [33]. As the indent depth increases, the fluctuation phenomenon on the subsequent *P-h* curve of the BCC + FCC1 can be observed, which means more dislocations are activated. It indicates that the alloy transits from the blocked to the unblocked state instantaneously during the deformation process via internal stress. Since the high density of the

FCC1 phase within the BCC matrix, the subsequent fluctuation phenomenon is also associated with the accumulation of dislocations in front of the semi-coherent interface between BCC and FCC1 phases, which instantaneously penetrates phase boundaries and causes local stress drop [34,35]. It indicates that BCC/FCC1 interface is energetically favored in enhancing the work hardening in the initial stage of plastic deformation. As shown in Fig. S4, the calculated hardening coefficient of the $(HfNbTaTiV)_{90}N_{10}$ alloy is 0.681, which is higher than that of the HfNbTaTiV alloy (0.316). However, pop-in events are severely suppressed in the curves of the FCC2 phase. The absence of pop-in events in the FCC2 is associated with intrinsic brittleness. Corresponding elastic modulus (*E*) and hardness are shown in Fig. 5(d). BCC and FCC2 phases exhibit the *E* of 171.8 and 228.6 GPa and hardness of 8.9 and 21.1 GPa, respectively. Due to the nanoscale grain size and high value of elastic modulus of the FCC1 phase, the BCC + FCC1 displays the highest elastic modulus of 276.2 GPa and the highest hardness of 25.8 GPa. Different elastic moduli of alternating phases will introduce extra forces in the softer phase, which promotes dislocation movement from the softer phase to the harder phase [18,36]. In dual-phase microstructure, the shear modulus (*G*) has momentous effects on the phase interfacial strengthening involving the dislocation-interface interaction [37]. The shear modulus can be derived as:

$$G = \frac{E}{2(1+\upsilon)} \tag{2}$$

where $\upsilon = 0.373$ is the Poisson's ratio for the studied $(HfNbTaTiV)_{90}N_{10}$ alloy [5,38]. The shear moduli of the BCC, BCC + FCC1, and FCC2 phases are calculated to be 62.6, 100.6, and 83.2 GPa, respectively. Both FCC1 and FCC2 phases exhibit a larger shear modulus than that of the BCC phase. The signifi-
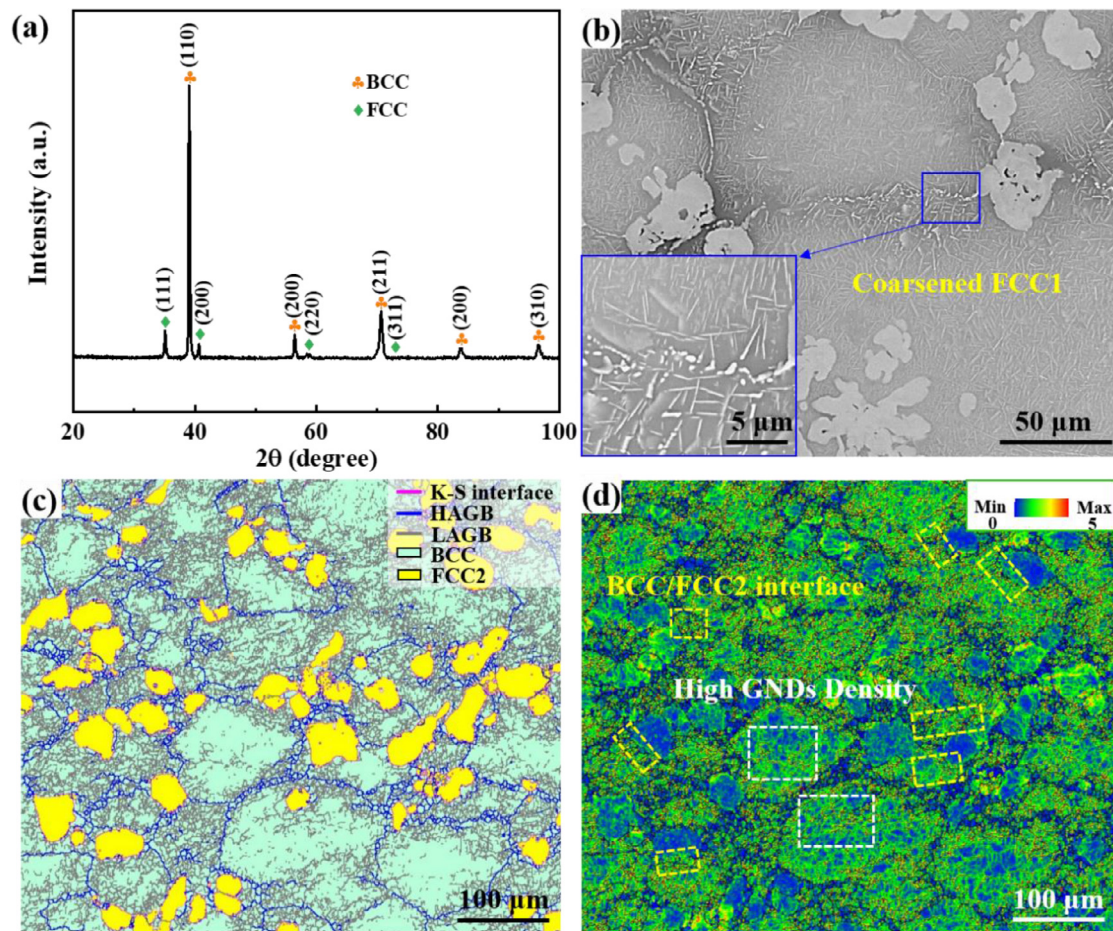
Fig. 6. Microstructure of (HfNbTaTiV)$_{90}$N$_{10}$ alloy after compressing at 1400 °C at the yield strain. (a) XRD pattern, (b) SEM image, (c) grain orientation difference distribution histogram, (d) KAM map.

cant shear modulus difference between the two phases increases the resistance of the phase interface to dislocation migration [18]. Therefore, the appearance of the FCC1 and FCC2 phases increases the strength of the (HfNbTaTiV)$_{90}$N$_{10}$ without significantly sacrificing ductility.

3.3. Microstructure evolution during deformation at 1400 °C

The microstructure of the (HfNbTaTiV)$_{90}$N$_{10}$ alloy after compressing to the yield point at 1400 °C is shown in Fig. 6. XRD pattern in Fig. 6(a) shows the same phase composition as at room temperature, demonstrating no phase transformation occurred during high-temperature compression. SEM characterization in Fig. 6(b) shows that the needle FCC1 and blocky FCC2 phases are retained. The blue rectangle area is enlarged and shown in the inset. Due to the enhanced atomic diffusion at high temperatures, only a small amount of needle FCC1 phases surrounded in the grain boundaries become coarsened, exhibiting a spherical morphology. It indicates that the (HfNbTaTiV)$_{90}$N$_{10}$ alloy has excellent structural stability during high-temperature deformation. The phase map obtained from EBSD is displayed in Fig. 6(c). The ratio of low-angle grain boundaries (LAGB) (2° to 10°) and high-angle grain boundaries (HAGB) represented by gray and blue lines are 76% and 24%, respectively. The deformation mainly occurs at the grain boundaries of the matrix and the interior of the BCC grains, which consists of large amounts of LAGBs. In contrast, the FCC1 and FCC2 phases exhibit excellent softening resistance with almost no deformation morphology. The appearance of HAGBs of the equiaxed grains in the BCC grain boundaries indicates the oc-

currence of recrystallization. A lower ratio of the HAGBs demonstrates that the FCC phase can effectively suppress the recrystallization softening of the BCC phase [14]. Besides, the FCC2 phases still maintain the K-S orientation relationship marked by the red lines with the matrix. It proves that the BCC matrix and FCC2 phase form a relatively stable interface structure to resist high-temperature deformation.

Due to the low energy of the semi-coherent interface, recrystallization grains tend to nucleate at the grain boundaries of the BCC matrix rather than at the interface. Since recrystallization effectively eliminates the stress concentration, the internal stress at the K-S interface is higher than that in the recrystallization region after high-temperature deformation. The corresponding KAM map is illustrated in Fig. 6(d), relatively high geometrically necessary dislocations (GNDs) density at K-S interfaces and within the deformed BCC grains are highlighted with yellow and white dash rectangles. High GNDs density at K-S interfaces demonstrates the gradients of plastic strain inside the BCC grains and in the K-S interface [19]. The results demonstrate that the FCC phase ensures the excellent high-temperature mechanical properties and phase stability of the (HfNbTaTiV)$_{90}$N$_{10}$ alloy.

4. Discussion

4.1. Effects of the semi-coherent interface on the strength-ductility combination

The interaction of dislocations at the interface plays a predominant role in the mechanical properties. To unveil the origin of the
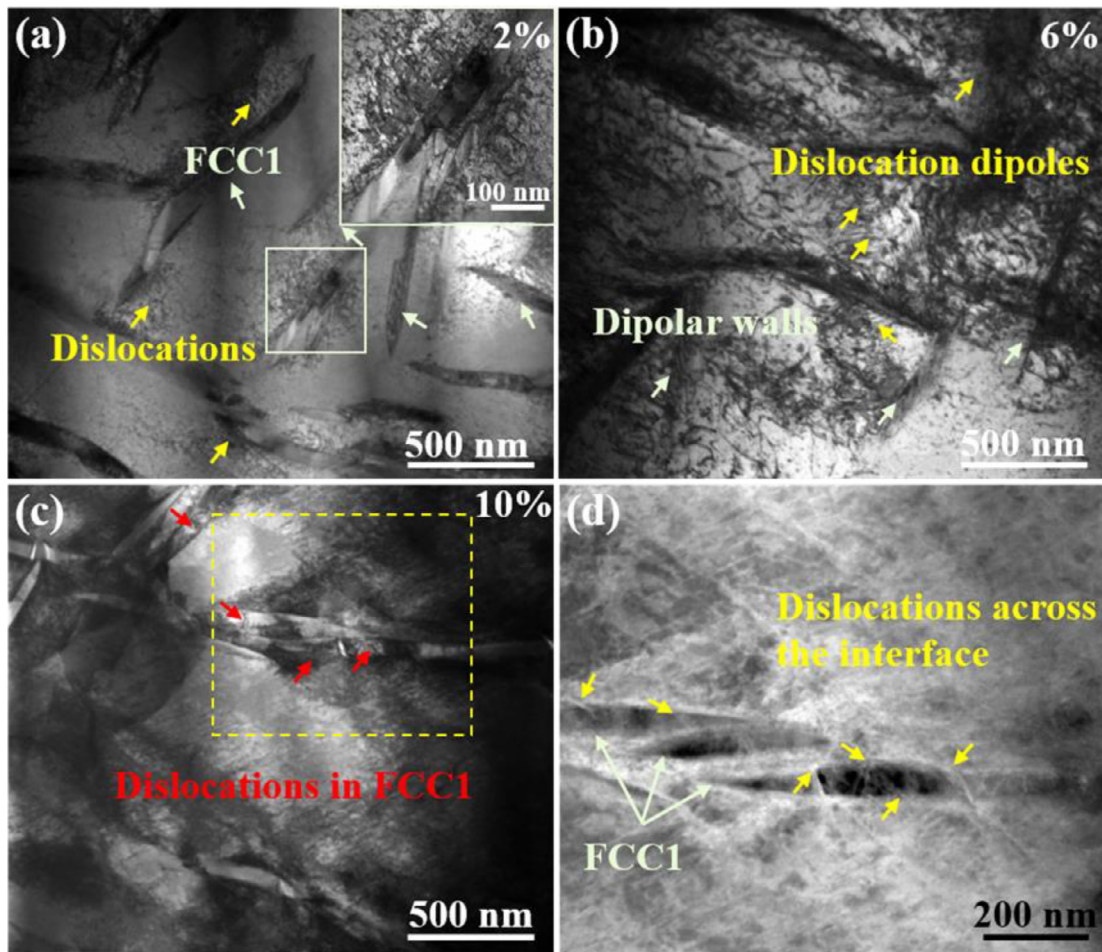
Fig. 7. STEM observation of dislocations in the (HfNbTaTiV)$_{90}$N$_{10}$ alloy in the deformation process at room temperature. (a) 2% strain, (b) 6% strain, (c) 10% strain, (d) enlarged HAADF-STEM of the yellow rectangle in (c).
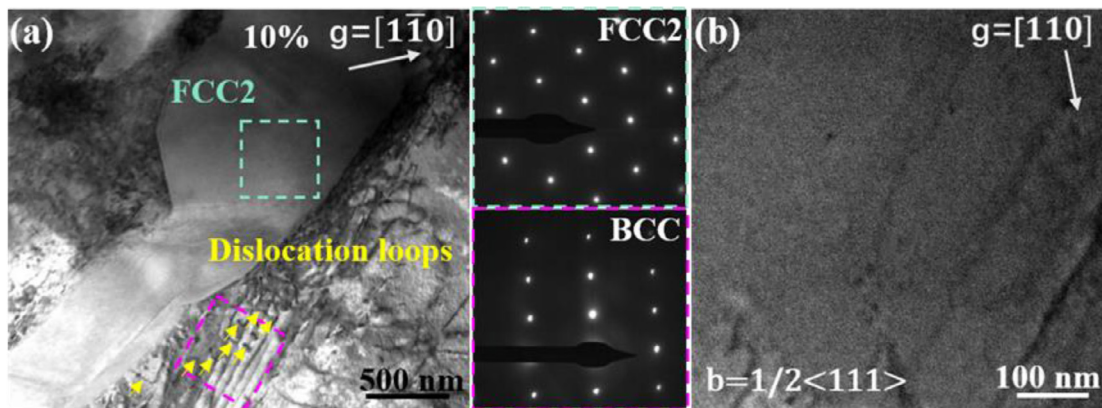

Fig. 8. Deformation around the FCC2 phase in the (HfNbTaTiV)$_{90}$N$_{10}$ alloy after 10% compression at room temperature using the two-beam diffraction with different **g** vectors. (a) **g** = [1$\bar{1}$0] and the corresponding SAED, (b) **g** = [110].

high strength and ductility of the (HfNbTaTiV)$_{90}$N$_{10}$ alloy, dislocation configurations are captured at the FCC1 phase in the BCC matrix area of the samples with the strain of 2%, 6%, and 10% after compressive tests at room temperature, as shown in Fig. 7. Fig. 7(a) displays the bright-field TEM image of the (HfNbTaTiV)$_{90}$N$_{10}$ with 2% strain. Dislocation density is low in the low-strained samples and the semi-coherent interface is the source of dislocation nucleation and emission. As shown in the illustration, the disloca-

tions initiate at the interface and extend to the BCC matrix. As the strain increases to 6%, dislocation dipoles and dipolar dislocation walls originating from the cross-slip of the screw dislocations are found, as shown in Fig. 7(b), indicating the plastic deformation of (HfNbTaTiV)$_{90}$N$_{10}$ is dominated by wavy slip. Dipolar walls emerge in the vicinity of FCC1, which promotes work hardening and ensures excellent ductility of the (HfNbTaTiV)$_{90}$N$_{10}$ alloy at ambient temperature [4]. Furthermore, a high density of dislocations was
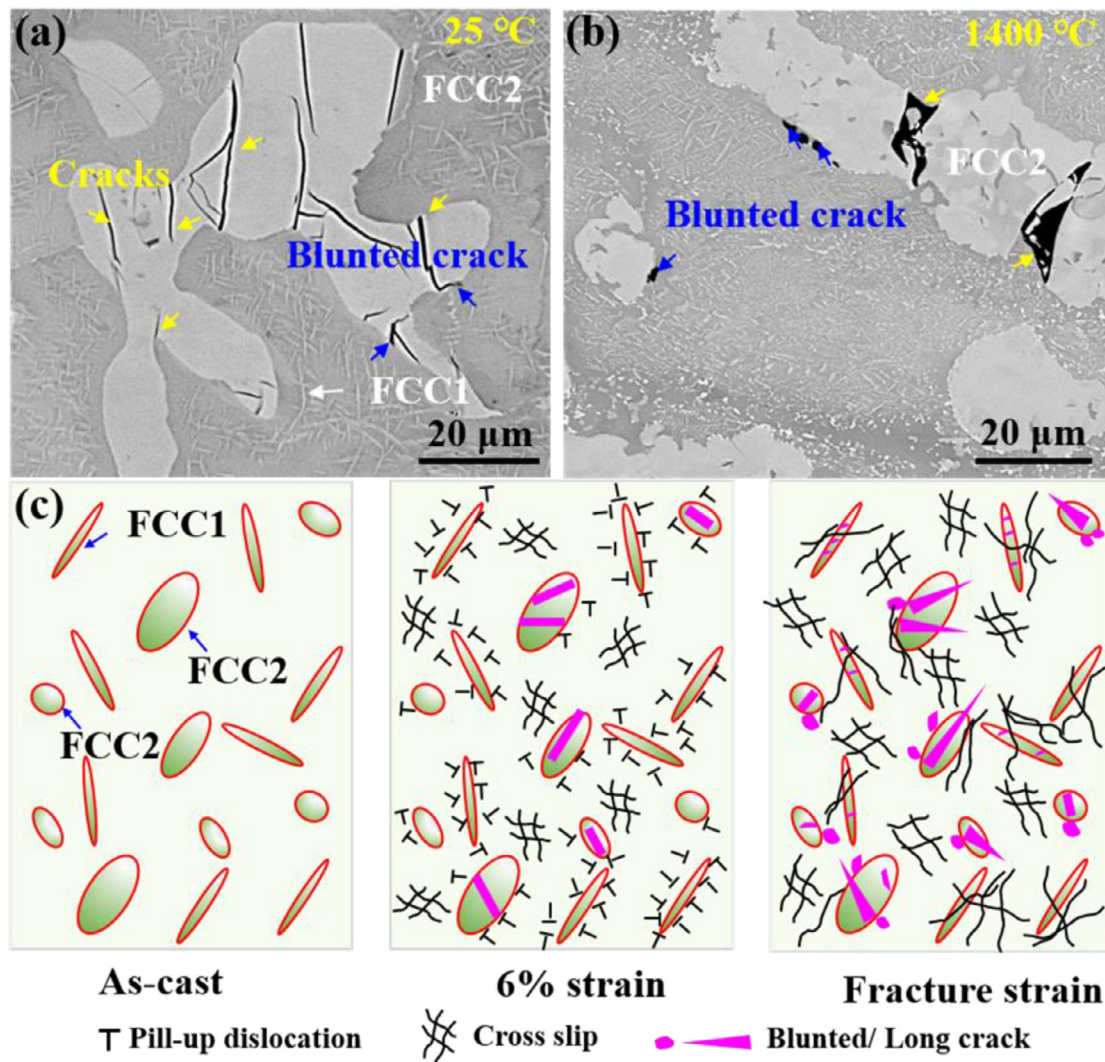
Fig. 9. Typical SEM images of cracks in the $(HfNbTaTiV)_{90}N_{10}$ alloy. (a) Compressed at ambient temperature with fracture strain, (b) Compressed at 1400 °C with 30% strain, multiple microcracks mainly including circle-like and tortuous are highlighted by yellow and blue arrows, respectively, (c) Schematic of the dislocation and microcrack-initiation behavior in the $(HfNbTaTiV)_{90}N_{10}$.

observed in the BCC phase, suggesting that the plastic deformation during initial deformation is mainly due to dislocation slippage in the BCC phase.

Fig. 7(c) displays the bright-field TEM image of the $(HfNbTaTiV)_{90}N_{10}$ alloy with 10% strain, the dislocation density increased rapidly. Massive dislocations (highlighted by the red arrow) can also be observed within the FCC1 phases. The entangled dislocations at a short distance show different dislocation densities, indicating the localization of plasticity in the FCC1 phase during the deformation process and the co-deformation of the BCC and FCC1 phases [19]. The enlarged view of the yellow rectangle in Fig. 7(c) is illustrated in Fig. 7(d). HAADF-STEM image shown in Fig. 7(d) demonstrates that partial dislocations are blocked on one side of the BCC/FCC1 interface, while others can cross the BCC/FCC1 interface (marked by the yellow arrow). The existence of the semi-coherent interface effectively reduces the stress concentration caused by dislocation pile-up [39]. Accordingly, the $(HfNbTaTiV)_{90}N_{10}$ alloy exhibits extremely high strength.

Fig. 8(a) is the bright-field image of the interface between BCC and FCC2 phases after compressing at room temperature with 10% strain and the corresponding SAED. Since the FCC2 with a large size cannot coordinate the deformation with the matrix, there are few dislocations within the FCC2 phase. High-density dislocations

are pinned at the interface of the BCC and FCC2 phases. Multiple dislocation entanglements can be observed. Partial dislocations move along the K-S interface in the same direction and are pinned by the BCC matrix, leaving a large number of dislocation loops (marked by a yellow arrow). There is no interaction between these dislocation loops, which promotes the nucleation and proliferation of dislocations. The cross slip of dislocations effectively alleviates strain localization in the plastic deformation [23,40]. Furthermore, no precipitation particle is found at the pinning position, indicating high lattice friction caused considerable resistance to dislocation glide in the BCC matrix, which is related to the pinning effects caused by chemical fluctuation in the $(HfNbTaTiV)_{90}N_{10}$ alloy.

The dislocations type near the BCC/FCC2 interface is identified by the extinction criterion $g \cdot b = 0$ and $g \cdot b \times u = 0$, where g and b are the operation reflection and Burgers vector, respectively [23], and u represents the direction of the dislocation line. Fig. 8(a) shows the morphology of the dislocations using the two-beam conditions with $g = [1\bar{1}0]$ in the $(HfNbTaTiV)_{90}N_{10}$ after 10% compression. It is completely invisible under $g = [110]$ along [001] zone axis in Fig. 8(b). Based on the extinction criterion, these dislocations in the BCC matrix are screw dislocations with the Burgers vector of $b = 1/2 \langle 111 \rangle$. The GND density ρ can be calculated according to the equation: $\rho = 2\sqrt{3}\varepsilon/db$, the grain di-

ameter d and micro-strain ε can be calculated from the XRD peak broadening (B) using the Williamsone-Hall equation [41]:

$$B\cos\theta_B = \frac{K\lambda}{d} + \varepsilon\sin\theta_B \qquad (3)$$

Here, θ_B is the Bragg angle, λ is the wavelength of Cu Kα radiation (0.154 nm), and K is constant. The values of dislocation density in the BCC matrix for $(HfNbTaTiV)_{90}N_{10}$ are calculated to be 4.71×10^{14} m^{-2}. This high density of dislocations in the BCC matrix can not only improve the yield strength but also improve the ductility through the proliferation and movement characteristics.

4.2. Crack-evolution mechanisms for the $(HfNbTaTiV)_{90}N_{10}$ alloy

The crack propagation in the $(HfNbTaTiV)_{90}N_{10}$ alloy after compression testing at 25 and 1400 °C are analyzed by SEM and shown in Fig. 9. As shown in Fig. 9(a), compressed at ambient temperature, the cracks in the $(HfNbTaTiV)_{90}N_{10}$ are found to initiate within the hard FCC2 phase rather than at phase boundaries or in the BCC phase. Consequently, the decrease in ductility is due to the intrinsic brittleness of the FCC2 phase [42]. The microstructure of the $(HfNbTaTiV)_{90}N_{10}$ after being compressed at 1400 °C with 30% strain is shown in Fig. 9(b). The morphology of the needle structure is retained. Multiple blunted microcracks mainly can be observed propagated at the BCC and FCC2 interfaces instead of large cracks, indicating that the BCC phase may attribute to retard the crack propagation by absorbing the strain energy around the crack tip and causing the crack blunting [12,24]. Therefore, the multiphase structure with alternating hard brittle, and softer phases is the key to the excellent combination of strength and ductility at room and high temperatures.

$(HfNbTaTiV)_{90}N_{10}$ alloy shows the same fracture mechanism at room temperature and high temperature. Crack evolution during the compression process can be schematically illustrated in Fig. 9(c). The $(HfNbTaTiV)_{90}N_{10}$ consists of BCC, FCC1, and FCC2 phases. Dislocations originate from the interface to activate the plastic deformation of the BCC phase in the initial deformation [18]. Despite the high strength and hardness of the FCC1, it can still undergo plastic deformation. It is distinct from the traditional intermetallic precipitates that cannot withstand too much plasticity. In addition, part of the dislocations can be transferred across the BCC/FCC1 interface. Certainly, due to the large size of the FCC2 phase, it is easy to initiate intrinsic microcracks. As the strain increases, the cross slip of screw dislocation effectively reduces the local stress and improves the ductility, which is beneficial to relieve the accumulation of damage caused by the deformation incompatibility between the BCC and FCC2 phases [39]. However, since the stress concentration near the interface intensifies, the dislocations no longer adapt to plastic deformation. Cracks in the FCC2 phase propagate into the matrix. The softer matrix delays crack propagation and results in blunting of the crack tip [24,42]. Blunted cracks with circles and tortuous morphology can be observed. Thereafter, cracks start to appear in the FCC1 phase as the deformation strain increases. Therefore, the $(HfNbTaTiV)_{90}N_{10}$ alloy with alternating softer and hard phases not only strengthens the BCC matrix but also coordinates the overall plastic deformation at ambient temperature.

5. Conclusion

In summary, nitride-reinforced HfNbTaTiV RHEA with ultrahigh strength and ductility at room and high temperatures was fabricated by arc melting. $(HfNbTaTiV)_{90}N_{10}$ is composed of the BCC matrix and FCC nitride phases. The semi-coherent interface between the BCC and FCC phases promotes the proliferation of dislocations and the cross slip of screw dislocations, which reduces the stress concentration and provides strong strain hardening. The nitride phase significantly improves the high-temperature softening resistance. Therefore, the $(HfNbTaTiV)_{90}N_{10}$ overcomes the strength-ductility trade-off at room temperature, showing ultrahigh yield strength of 2716 MPa and large plasticity of 10%. Besides, the alloy exhibits a high yield strength of 639 MPa at 1200 °C and 279 MPa at 1400 °C. No phase transformation appeared after high-temperature compressing, which indicates the excellent high temperature stability. $(HfNbTaTiV)_{90}N_{10}$ with a multiphase heterogeneous structure realizes the coordinated deformation of the high melting point hard nitride phase and the high-entropy metallic phase. The alloy with low density exhibits high strength and large ductility at room temperature, providing a new strategy to solve the brittleness of RHEAs at ambient temperature.

Declaration of Competing Interest

The authors report no declarations of interest.

Acknowledgments

Supplementary materials

Supplementary material associated with this article can be found, in the online version, at doi:10.1016/j.jmst.2022.12.010.

References

[1] D.B. Miracle, O.N. Senkov, Acta Mater. 122 (2017) 448–511.
[2] Y.X. Wan, X. Wang, Z.B. Zhang, J.Y. Mo, B.L. Shen, X.B. Liang, J. Alloy. Compd. 889 (2021) 161645.
[3] O. Senkov, J. Scott, S. Senkova, F. Meisenkothen, D. Miracle, C. Woodward, J. Mater. Sci. 47 (2012) 4062–4074.
[4] Z.F. Lei, X.J. Liu, Y. Wu, H. Wang, S.H. Jiang, S.D. Wang, X.D. Hui, Y.D. Wu, B. Gault, P. Kontis, D. Raabe, L. Gu, H.W. Chen, H.T. Wang, J.B. Liu, K. An, Q.S. Zeng, T.G. Nieh, Z.P. Lu, Nature 563 (2018) 546–550.
[5] B.J. Wang, Q.Q. Wang, N. Lu, X.B. Liang, B.L. Shen, J. Mater. Sci. Technol. 123 (2022) 191–200.
[6] M. Song, R. Zhou, J. Gu, Z.W. Wang, S. Ni, Y. Liu, Appl. Mater. Today 18 (2020) 100498.
[7] Y.P. Lu, X.Z. Gao, L. Jiang, Z.N. Chen, T.M. Wang, J.C. Jie, H.J. Kang, Y.B. Zhang, S. Guo, H.H. Ruan, Y.H. Zhao, Z.Q. Cao, T.J. Li, Acta Mater. 124 (2017) 143–150.
[8] P.J. Shi, W.L. Ren, T.X. Zheng, Z.M. Ren, X.L. Hou, J.C. Peng, P.F. Hu, Y.F. Gao, Y.B. Zhong, P.K. Liaw, Nat. Commun. 10 (2019) 489.
[9] B. Gwalani, S. Gorsse, D. Choudhuri, M. Styles, Y. Zheng, R.S. Mishra, R. Banerjee, Acta Mater. 153 (2018) 169–185.
[10] F. Otto, A. Dlouhý, K.G. Pradeep, M. Kubenov, D. Raabe, G. Eggeler, E.P. George, Acta Mater. 112 (2016) 40–52.
[11] Z. Jiang, R. Wei, W.Z. Wang, M.J. Li, Z.H. Han, S.H. Yuan, K.S. Zhang, C. Chen, T. Wang, F.S. Li, J. Mater. Sci. Technol. 100 (2022) 20–26.
[12] S.S. Sohn, D.G. Kim, Y.H. Jo, A.K.D. Silva, W.J. Lu, A.J. Breen, B. Gault, D. Ponge, Acta Mater. 194 (2020) 106–117.
[13] X.Z. Gao, Y.P. Lu, B. Zhang, N.N. Liang, G.Z. Wu, G. Sha, J.Z. Liu, Y.H. Zhao, Acta Mater. 141 (2017) 59–66.
[14] T.J. Jang, W.S. Choi, D.W. Kim, G. Choi, H. Jun, A. Ferrari, F. Körmann, P.P. Choi, S.S. Sohn, Nat. Commun. 12 (2021) 4703.
[15] Q.Q. Wei, G.Q. Luo, R. Tu, J. Zhang, Q. Shen, Y.J. Cui, Y.W. Gui, A. Chiba, J. Mater. Sci. Technol. 84 (2021) 1–9.
[16] Y.X. Ye, B. Ouyang, C.Z. Liu, G.J. Duscher, T.G. Nieh, Acta Mater. 199 (2020) 413–424.
[17] I. Moravcik, H. Hadraba, L.L. Li, I. Dlouhy, D. Raabe, Z.M. Li, Scr. Mater. 178 (2020) 391–397.
[18] T. Xiong, W.F. Yang, S.J. Zheng, Z.R. Liu, Y.P. Lu, R.F. Zhang, Y.T. Zhou, X.H. Shao, B. Zhang, J. Wang, F.X. Yin, P.K. Liaw, X.L. Ma, J. Mater. Sci. Technol. 65 (2021) 216–227.
[19] Y.M. Zhang, C.Y. Wang, K.M. Reddy, W. Li, X.D. Wang, Acta Mater. 226 (2022) 117670.
[20] P.A. Rad, P. Sathiyamoorthi, N.T.C. Nguyen, A. Zargaran, T.S. Kim, H.S. Kim, Scr. Mater. 190 (2021) 69–74.
[21] K.J. Lu, A. Chauhan, D. Litvinov, A.S. Tirunilai, J. Freudenberger, A. Kauffmann, M. Heilmaier, J. Aktaa, J. Mater. Sci. Technol. 100 (2022) 237–245.
[22] Q.Q. Ding, Y. Zhang, X. Chen, X.Q. Fu, D.K. Chen, S.J. Chen, L. Gu, F. Wei, H.B. Bei, Y.F. Gao, M.R. Wen, J.X. Li, Z. Zhang, T. Zhu, R.O. Ritchie, Q. Yu, Nature 574 (2019) 223–227.

[23] Y.Q. Bu, Y. Wu, Z.F. Lei, X.Y. Yuan, H.H. Wu, X.B. Feng, J.B. Liu, J. Ding, Y. Lu, H.T. Wang, Z.P. Lu, W. Yang, Mater. Today 46 (2021) 28–34.

[24] Q.Q. Wei, X.D. Xu, G.M. Li, G.Q. Luo, J. Zhang, Q. Shen, C.L. Wu, Scr. Mater. 200 (2021) 113909.

[25] S.Y. Wu, D.X. Qiao, H.T. Zhang, J.W. Miao, H.L. Zhao, J. Wang, Y.P. Lu, T.M. Wang, T.J. Li, J. Mater. Sci. Technol. 97 (2022) 229–238.

[26] O.N. Senkov, S. Gorsse, D.B. Miracle, Acta Mater. 175 (2019) 394–405.

[27] Y. Zhang, Y. Liu, Y. Li, X. Chen, H. Zhang, Mater. Lett. 174 (2016) 82–85.

[28] O.N. Senkov, D.B. Miracle, K.J. Chaput, J.P. Couzinie, J. Mater. Res. 33 (2018) 3092–3128.

[29] Z.Q. Wang, H.H. Wu, Y. Wu, H.L. Huang, X.Y. Zhu, Y.J. Zhang, H.H. Zhu, X.Y. Yuan, Q. Chen, S.D. Wang, X.J. Liu, H. Wang, S.H. Jiang, M.J. Kim, Z.P. Lu, Mater. Today 54 (2022) 83–89.

[30] N.N. Guo, L. Wang, L.S. Luo, X.Z. Li, Y.Q. Su, J.J. Guo, H.Z. Fu, Mater. Des. 81 (2015) 87–94.

[31] Q.Q. Wei, Q. Shen, J. Zhang, Y. Zhang, G.Q. Luo, L.M. Zhang, J. Alloy. Compd. 777 (2019) 1168–1175.

[32] E. Ma, T. Zhu, Mater. Today 20 (2017) 323–331.

[33] K.F. Gan, D.S. Yan, S.Y. Zhu, Z.M. Li, Acta Mater. 206 (2021) 116633.

[34] B.B. He, Z.Y. Liang, M.X. Huang, Scr. Mater. 150 (2018) 134–138.

[35] S.J. Lu, B. Zhang, X.Y. Li, J.W. Zhao, M. Zaiser, H.D. Fan, X. Zhang, J. Mech. Phys. Solids 126 (2019) 117–135.

[36] S.I. Rao, P.M. Hazzledine, D.M. Dimiduk, Mater. Res. Soc. Symp. Proc. 362 (1995) 67–77.

[37] G. Qin, R. Chen, P.K. Liaw, Y.F. Gao, X.Q. Li, H.T. Zheng, L. Wang, Y.Q. Su, J.J. Guo, H.Z. Fu, Scr. Mater. 172 (2019) 51–55.

[38] Z.B. An, S.C. Mao, Y.N. Liu, L. Wang, H. Zhou, B. Gan, Z. Zhang, X.D. Han, J. Mater. Sci. Technol. 79 (2021) 109–117.

[39] R. Feng, Y. Rao, C.H. Liu, X. Xie, D.J. Yu, Y. Chen, M. Ghazisaeidi, T. Ungar, H.M. Wang, K. An, P.K. Liaw, Nat. Commun. 12 (2021) 3588.

[40] W.G. Nohring, W.A. Curtin, Acta Mater. 158 (2018) 95–117.

[41] G.K. Williamson, W.H. Hall, Acta Metall. 1 (1953) 22–31.

[42] L.L. Han, X.D. Xu, L. Wang, F. Pyczak, R. Zhou, Y. Liu, Mater. Res. Lett. 7 (2019) 460–466.